

## Electronic Supplementary Information

### 3D cuboidal vanadium diselenide embedded reduced graphene oxide hybrid structures with enhanced supercapacitor properties

Subba R. Marri,<sup>a,#</sup> Satyajit Ratha,<sup>b,#</sup> Chandra Sekhar Rout\* and J. N. Behera\*

---

<sup>a</sup> School of Chemical Science, National Institute of Science Education and Research (NISER), Jatni 752050, India, E-mail: [jnbehera@niser.ac.in](mailto:jnbehera@niser.ac.in)

<sup>b</sup> School of Basic Sciences, Indian Institute of Technology, Bhubaneswar 751013, India E-mail: [csrout@iitbbs.ac.in](mailto:csrout@iitbbs.ac.in), [csrout@gmail.com](mailto:csrout@gmail.com)

#### Experimental section

**Synthesis of GO and RGO:** GO was synthesized by a modified Hummer's method as provided in an earlier report.<sup>1</sup> Reduction of GO to RGO took place after the hydrothermal reaction at 200 °C for 24 h.

**Synthesis of VSe<sub>2</sub> and VSe<sub>2</sub>/RGO hybrids:** VSe<sub>2</sub> layers were synthesized by a method reported elsewhere with slight modification.<sup>2</sup> In a typical process, 40.6 mg of sodium metavanadate (NaVO<sub>3</sub>, Sigma Aldrich) and 74 mg of Selenium dioxide were dissolved together in 5 ml of DI water by constant stirring. The volume of the mixture solution was increased to 14 ml by adding DI water after which 1 ml of formic acid was slowly added to the above mixture solution. After thorough stirring, the mixture solution was transferred to a Teflon-lined stainless steel autoclave of 23 ml capacity and kept inside an oven at 200 °C for 24 h. After the completion of hydrothermal reaction, the pure black precipitate of VSe<sub>2</sub> was collected via filtration and washed repeatedly with water and absolute ethanol. After thorough washing, the precipitate was dried in vacuum at 60 °C for 24 h.

VSe<sub>2</sub>/RGO hybrids were synthesized by the same hydrothermal method described above with only difference that the vanadium and selenium precursors were dissolved directly in a uniform aqueous dispersion of GO (at different concentrations, i.e. 0.15, 0.3, and 0.75 wt%). Reduction of GO to RGO occurred during the hydrothermal process.

#### Characterization

Morphology of the samples were studied with the help of field emission scanning electron microscopy (Merlin Compact with Gemini-I electron column, Zeiss Pvt. Ltd., Germany).

Elemental analyses and energy dispersive X-ray spectroscopy (INCA, Oxford Instruments, UK) were employed to check the elemental composition of the samples. Intrinsic morphology was studied with the help of transmission electron microscopy (JEOL 3010, operates at 300 kV) Oxidation states of the samples were investigated using X-ray photoemission spectroscopy (Scienta Omicron ESCA) technique.

### **Electrochemical supercapacitor study**

**Device fabrication:** Detailed investigation regarding supercapacitor performance of the samples was done using a standard Potentiostat/Galvanostat (Technoscience Instruments, Bangalore, India). The supercapacitor device was fabricated using a CR2032 type coin cell arrangement. In a typical process, ink like slurry was prepared by thoroughly dispersing the sample in viable amount of acetonitrile in a bath sonicator for 15-20 minutes. The as prepared slurry was then coated on to the surface of a nickel foil (pre-treated with 1M HCl) with the help of a desktop coating machine so as to achieve a mass loading of  $\sim 2$  mg for each symmetric electrode. A screw gauge arrangement ensured control over the coating process in order to get desired uniform film thickness. The sample modified foil was then hot roll pressed at 100 °C resulting in better adherence between sample and the foil. After that the sample modified foil was cut into circular shapes of pre-defined size using a disc cutter. These circular shaped modified foils were then used as the electrodes for supercapacitor testing. A cellulose nitrate membrane having pore size of  $\sim 0.22$   $\mu$  (HiMedia Laboratories Pvt. Ltd., India) was used as the separator and 0.5 M aqueous solution of  $K_2SO_4$  was used as the electrolyte. Mass loading of the sample was calculated by comparing a modified and bare nickel foil of the same dimension. For hybrid samples, cyclic voltammetry, constant current charge-discharge measurement, and cyclic stability measurements were performed within a potential window of 1.5 V (from 0.0 V to 1.5 V) and for  $VSe_2$ , RGO, the potential window was set to 1V (from 0.0 V to 1.0 V). Corresponding cyclic voltammograms, charge-discharge curves and long cycle stability data were obtained and supercapacitor performance of the sample was evaluated.

### **Electrochemical impedance spectroscopy (EIS)**

EIS on the as-fabricated coin cell type symmetric supercapacitors was done with the help of Autolab PGSTAT100N. An input sinusoidal AC signal (having very small amplitude of 5 mV to preserve pseudo-linearity) was applied to the coin cell type supercapacitor within a frequency

range of 0.05 Hz-100 kHz. The output result was obtained through Nyquist plot showing both the real (resistance) and imaginary (capacitance) parts of the device impedance.

### **BET surface area analyses**

The average surface areas of VSe<sub>2</sub> and V/G\_0.3 were investigated via BET surface area analysis with the help of Quantachrome® ASiQwin™ (version 3.01) Instrument.

### **Calculation of specific capacitance ( $C_{SP}$ ), energy density ( $E_d$ ) and power density ( $P_d$ ):**

Specific capacitance from cyclic voltammetry was derived by following a method detailed in a previous report;<sup>3</sup>

$$C_{SP} = \frac{\int_{V_i}^{V_f} I(V)dV + \int_{V_f}^{V_i} I(V)dV}{2mr(V_f - V_i)} \quad (1)$$

where,  $V_f$  and  $V_i$  are final and initial values of the working potential window, the summed integral in the numerator denotes the total absolute area under the CV curve,  $m$  is the mass of the electrode material, and  $r$  is the rate of potential sweep.

From the charge-discharge (CD) measurement data, specific capacitance was calculated by using the following equation;

$$C_{SP} = \frac{I}{m \frac{dV}{dt}} \quad (2)$$

Where,  $m$  is the mass of the electrode,  $\frac{dV}{dt}$  is the slope of the discharge curve, and  $I$  is the discharge current. Energy density ( $E_d$ ) and power density ( $P_d$ ) of the samples were calculated by using the following equations.

$$E_d = \frac{1}{2} C_{SP} (\Delta V)^2 \quad (2)$$

$$P_d = \frac{E_d}{t_d} \quad (3)$$

Where,  $\Delta V (V_f - V_i)$  represents the working potential window and  $t_d$  is the discharge time.

### **Growth mechanism behind the formation of VSe<sub>2</sub> cuboid structures:**

The presence of graphene oxide in hydrothermal reactions provides immediate and favorable sites for ad-atoms and triggers nucleation process minimizing the occurrence of free formed particles.<sup>4-8</sup> In many such previously reported hybrids,<sup>4-8</sup> the mechanism can be explained in terms of the strong coupling between the metal ions (typically of the transition group having multiple oxidation states) and the oxygenated functional groups present in the graphene oxide (in the basal plane and also at edges). Thus graphene as a template plays significant role in the growth, nucleation, and shape modification of the resultant composites. Furthermore, it has been found that three dimensional structures are favored in hydrothermal reactions involving inorganic materials facilitated by high degree of supersaturation.<sup>7</sup> Though nucleation and growth occurs in a standard hydrothermal synthesis, however, in the presence of GO both diffusion and recrystallization is greatly suppressed.<sup>7</sup> In our report, three composites of VSe<sub>2</sub> and reduced graphene oxide (i.e. V/G\_0.15, V/G\_0.3, and V/G\_0.75) have been reported. In the case of V/G\_0.15, although stacking of VSe<sub>2</sub> can be observed (Fig. S4a), no matured cuboid structures were found. This could have been due to the low wt% of GO in the reaction mixture. V/G\_0.3 sample showed prominent VSe<sub>2</sub> cuboids (Fig. 1a) due to the presence of GO in comparatively higher concentration/wt%. Growth and nucleation of VSe<sub>2</sub> similar to that of V/G\_0.3 was also found in the case of V/G\_0.75. However, due to excessive wt%, the GO layers formed agglomerations which wrapped up significant numbers of VSe<sub>2</sub> cuboids blocking their active surfaces. A schematic has been provided (Fig. S1) to illustrate the mechanism behind the formation of VSe<sub>2</sub> cuboids in the presence of GO as an active template. In the first step, the hydrolyzed precursor release  $VO_3^-$  which is readily adsorbed onto the defect sites (having oxygenated functional groups) present on the graphene oxide. Second step involves growth due

to supersaturation and formation of favorable facet which facilitates further oriented growth to form three dimensional structures. In the third step, the hybrid having  $\text{VSe}_2$  cuboids embedded into the reduced graphene oxide layers has been illustrated.

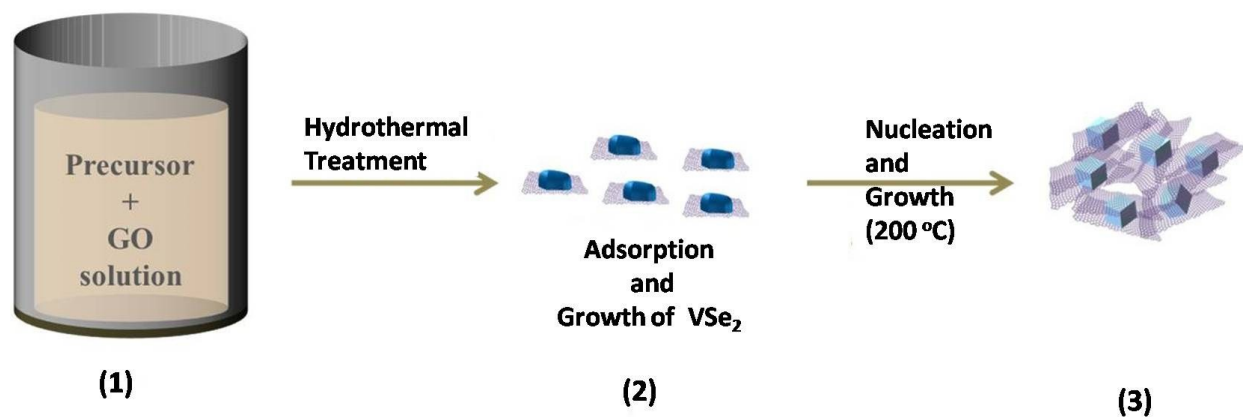


**Fig. S1** Schematic representation of the growth and formation of  $\text{VSe}_2$  cuboids in the presence of reduced graphene oxide during the hydrothermal treatment.

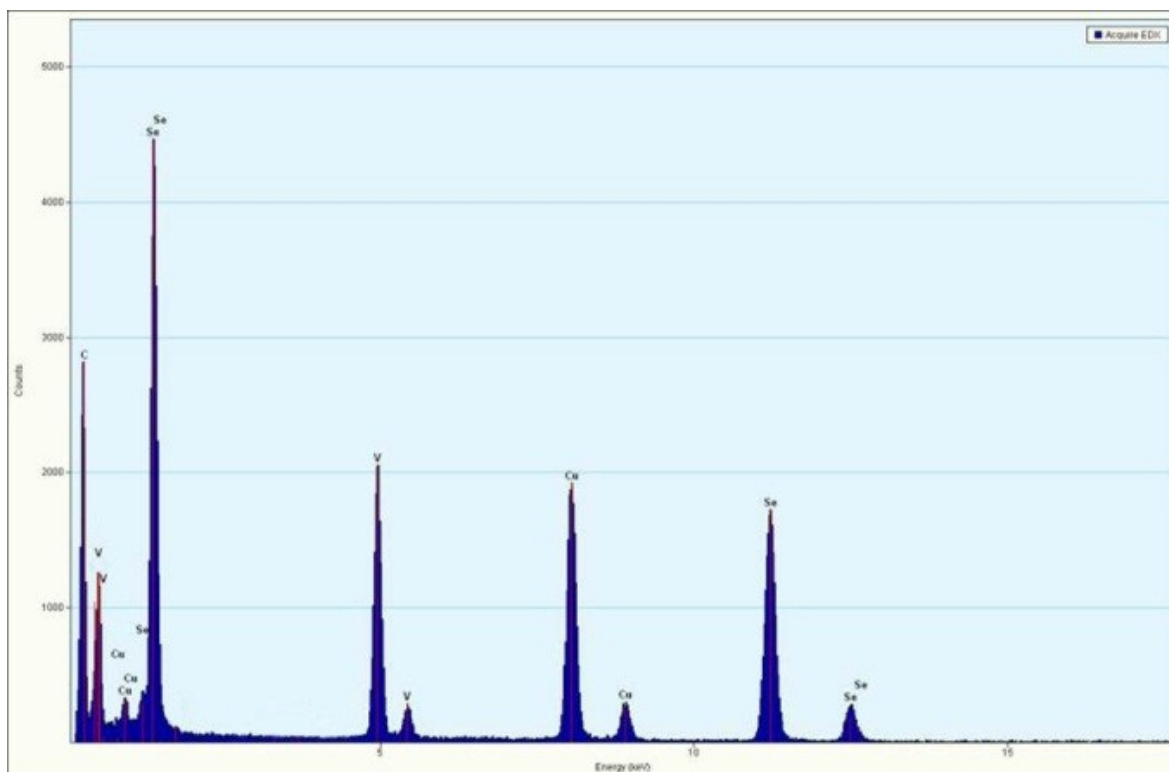


**Fig. S2** EDS on TEM done for V/G\_0.3 showing the peaks corresponding to C, O, V, and Se confirming the presence of RGO and  $VSe_2$ .

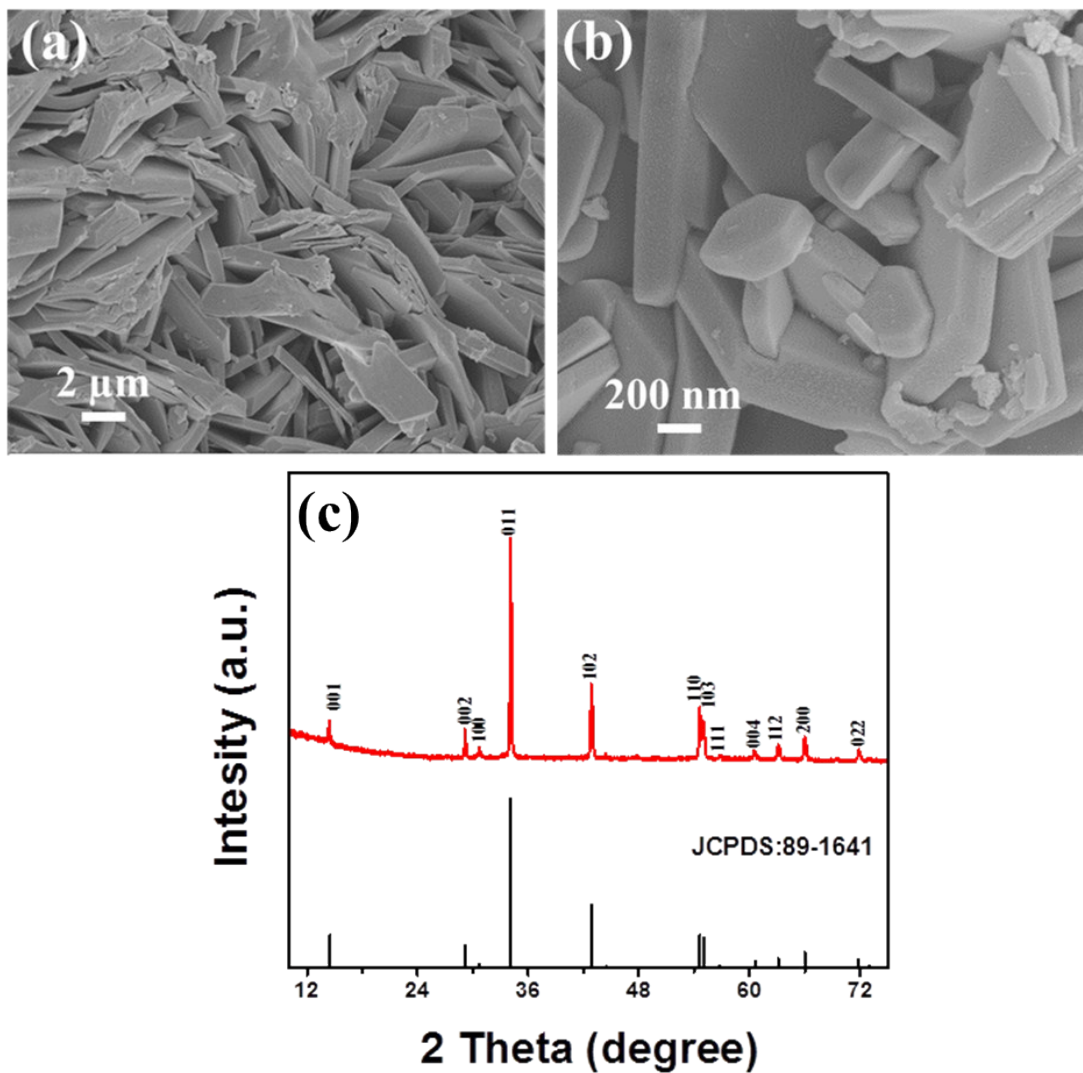


**Fig. S3** (a) Low and (b) high magnification FESEM images and (c) powder X-ray diffraction of pristine VSe<sub>2</sub> sample.

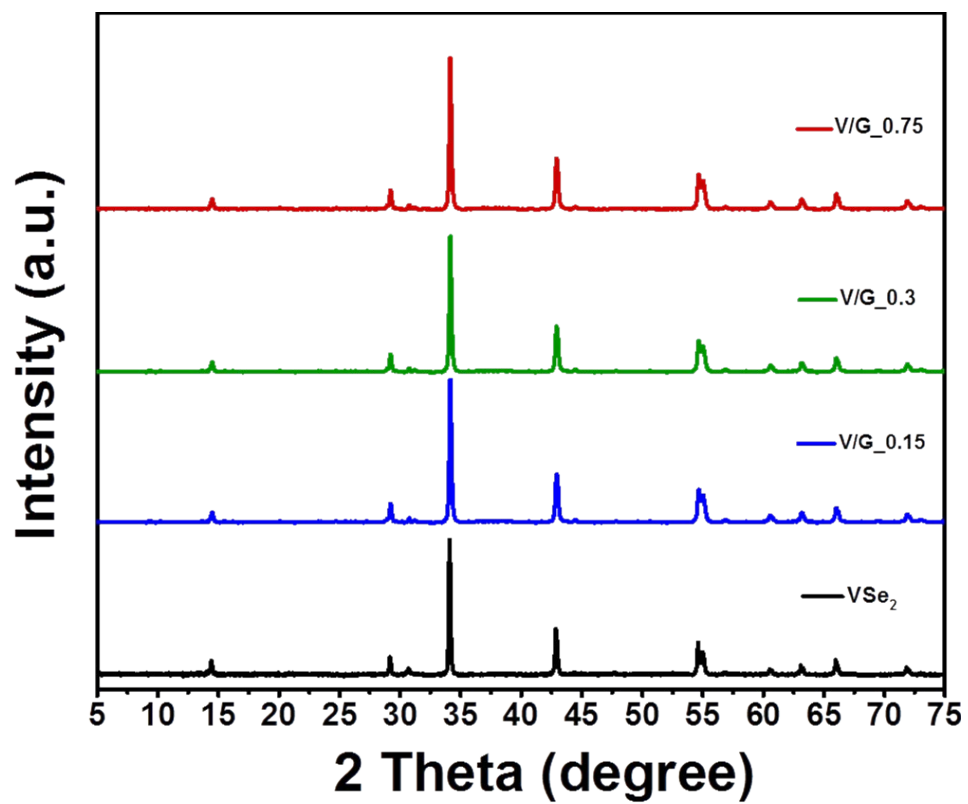


**Fig. S4** Comparison of powder XRD spectra obtained from VSe<sub>2</sub>, V/G\_0.15, V/G\_0.3, and V/G\_0.75.

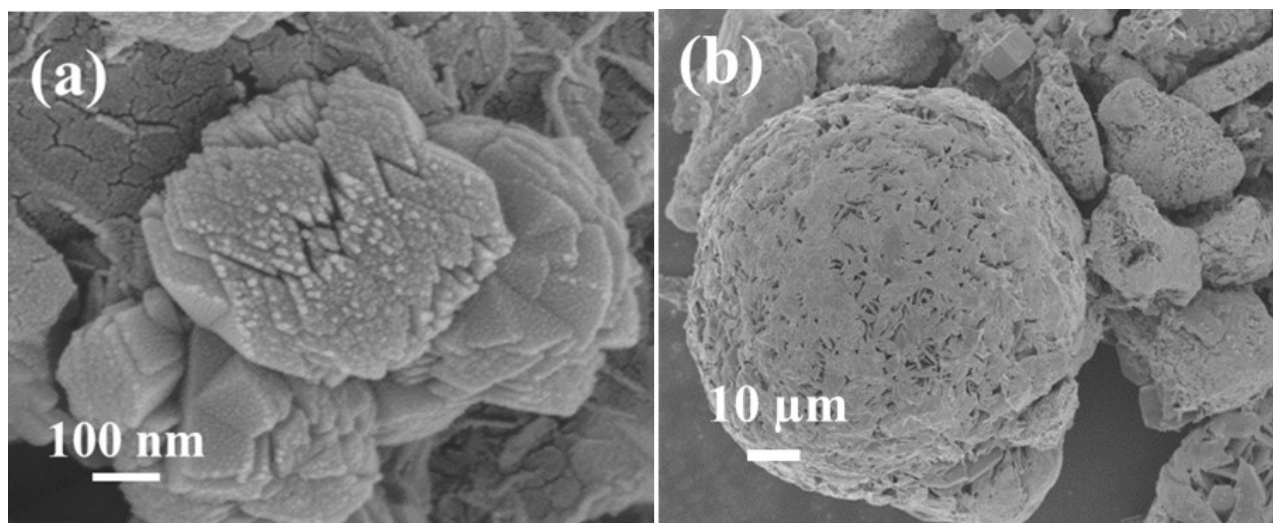


**Fig. S5** FESEM images of (a) V/G\_0.15 and (b) V/G\_0.75 hybrids.

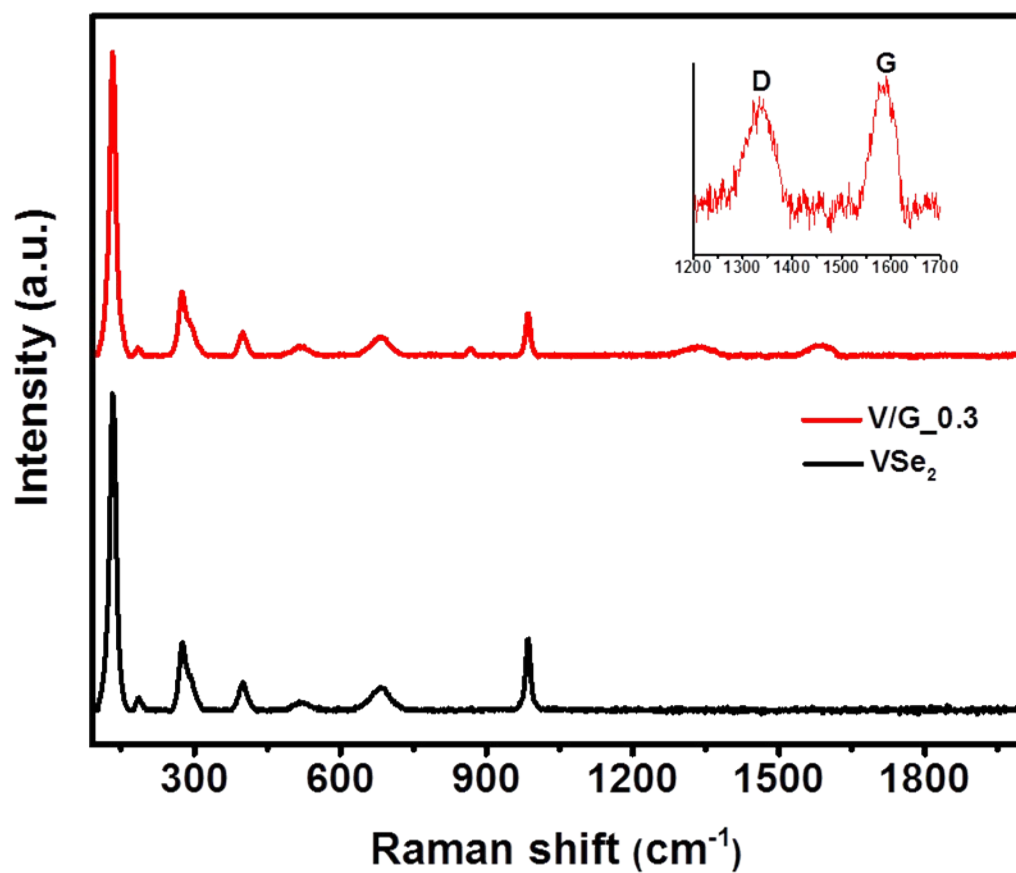


**Fig. S6** Comparison of Raman spectra obtained from VSe<sub>2</sub>, and V/G\_0.3. The inset obtained from V/G\_0.3 shows the characteristic D and G band of RGO.

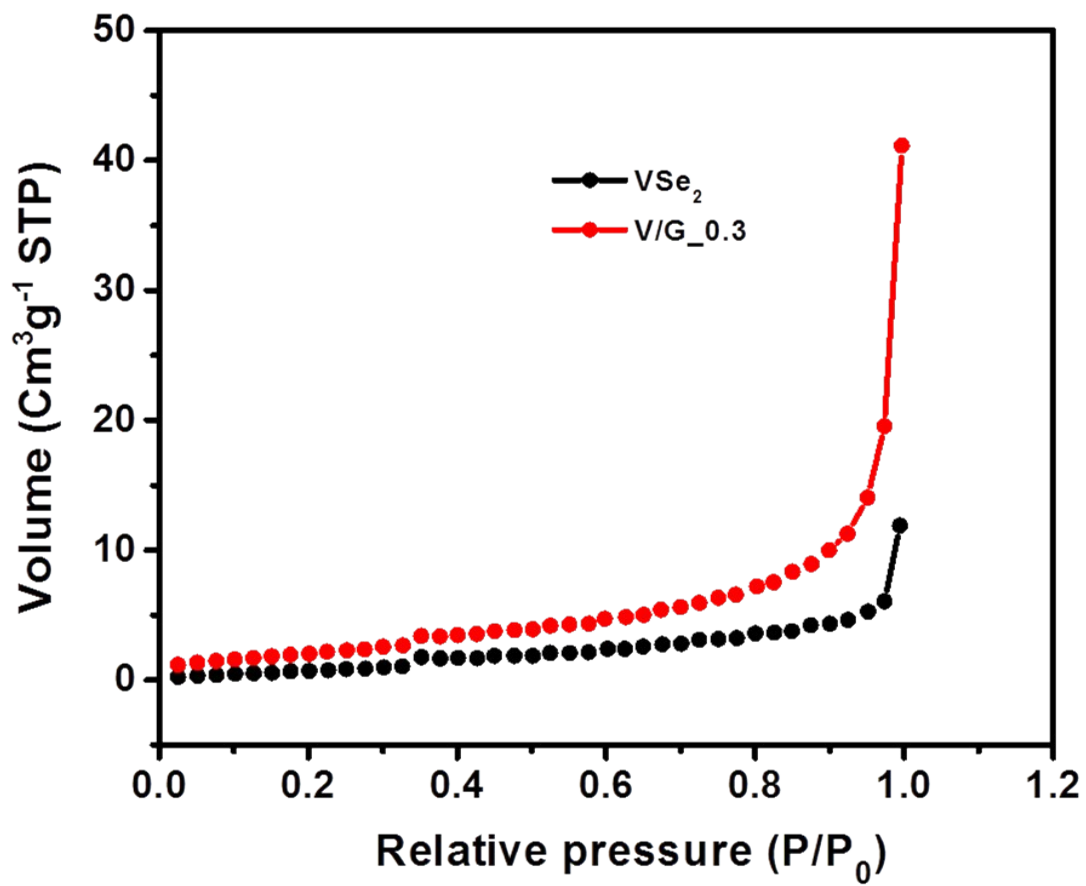
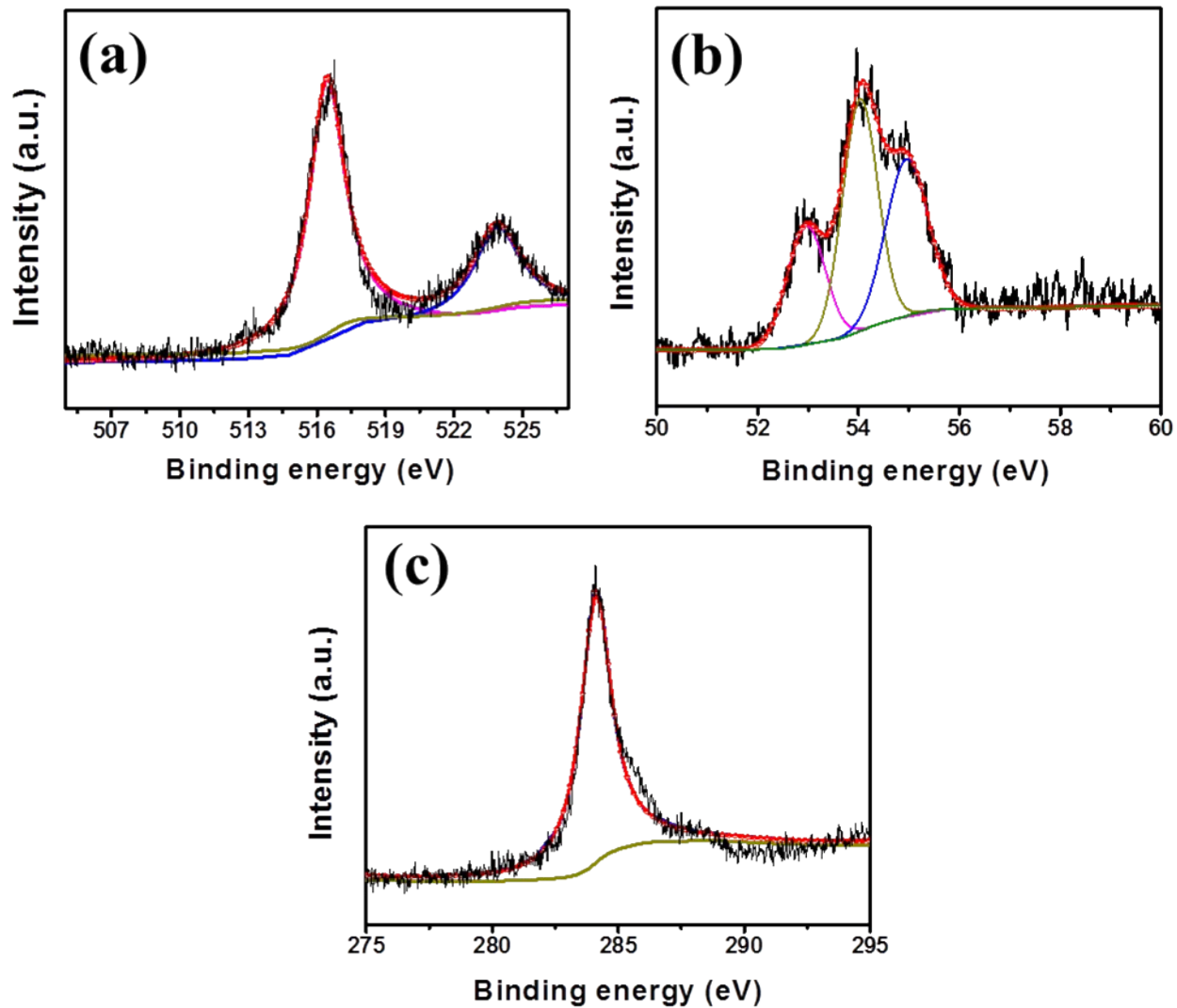
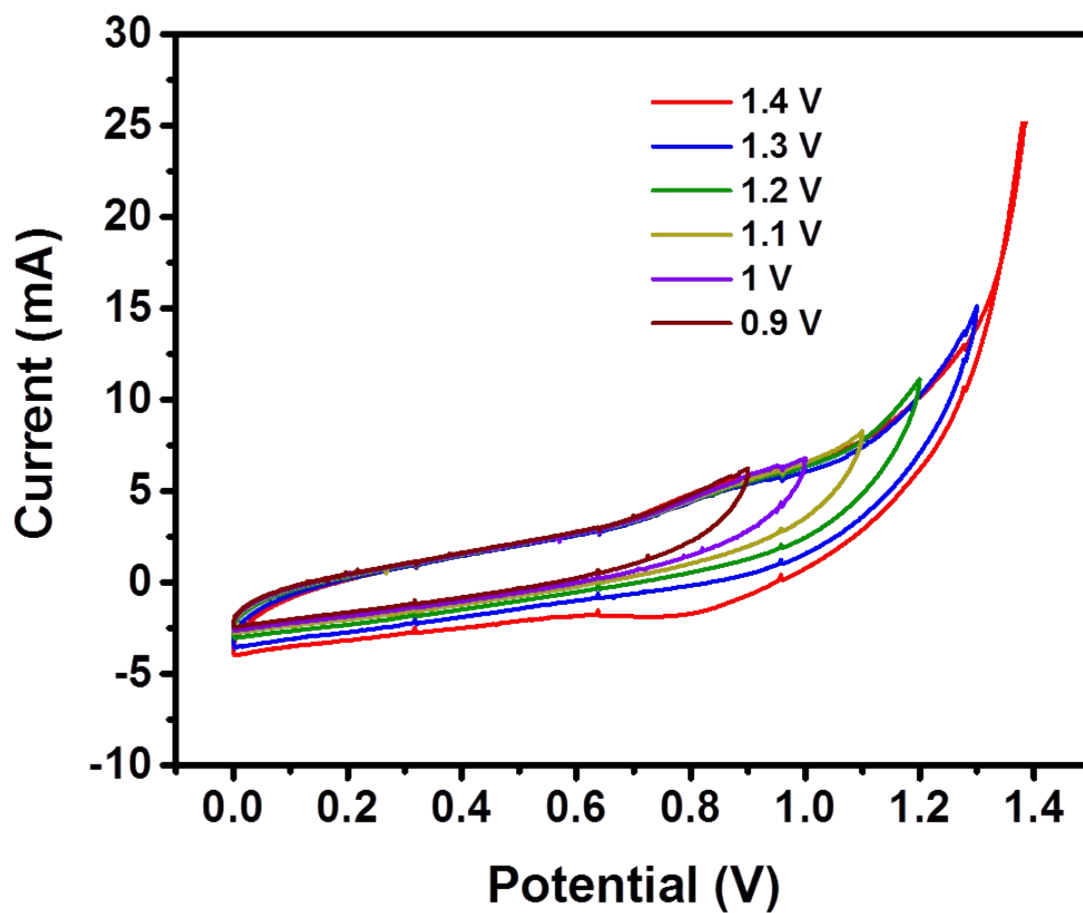


Fig. S7 Plot showing comparison of results of BET analyses on VSe<sub>2</sub> and V/G\_0.3.



**Fig. S8** X-ray photoelectron data for V/G\_0.3 shows (a)  $2p_{3/2}$  and  $2p_{1/2}$  core level of vanadium, (b) 3d core level of selenium, and (c) C1s spectra originating from RGO.



**Fig. S9** Comparison of cyclic voltammograms for VSe<sub>2</sub> obtained at various working potential window. At ~1.1 V, onset of oxygen evolution process can be observed and therefore a working potential window of 1V was taken for measuring the supercapacitor performance of VSe<sub>2</sub>.

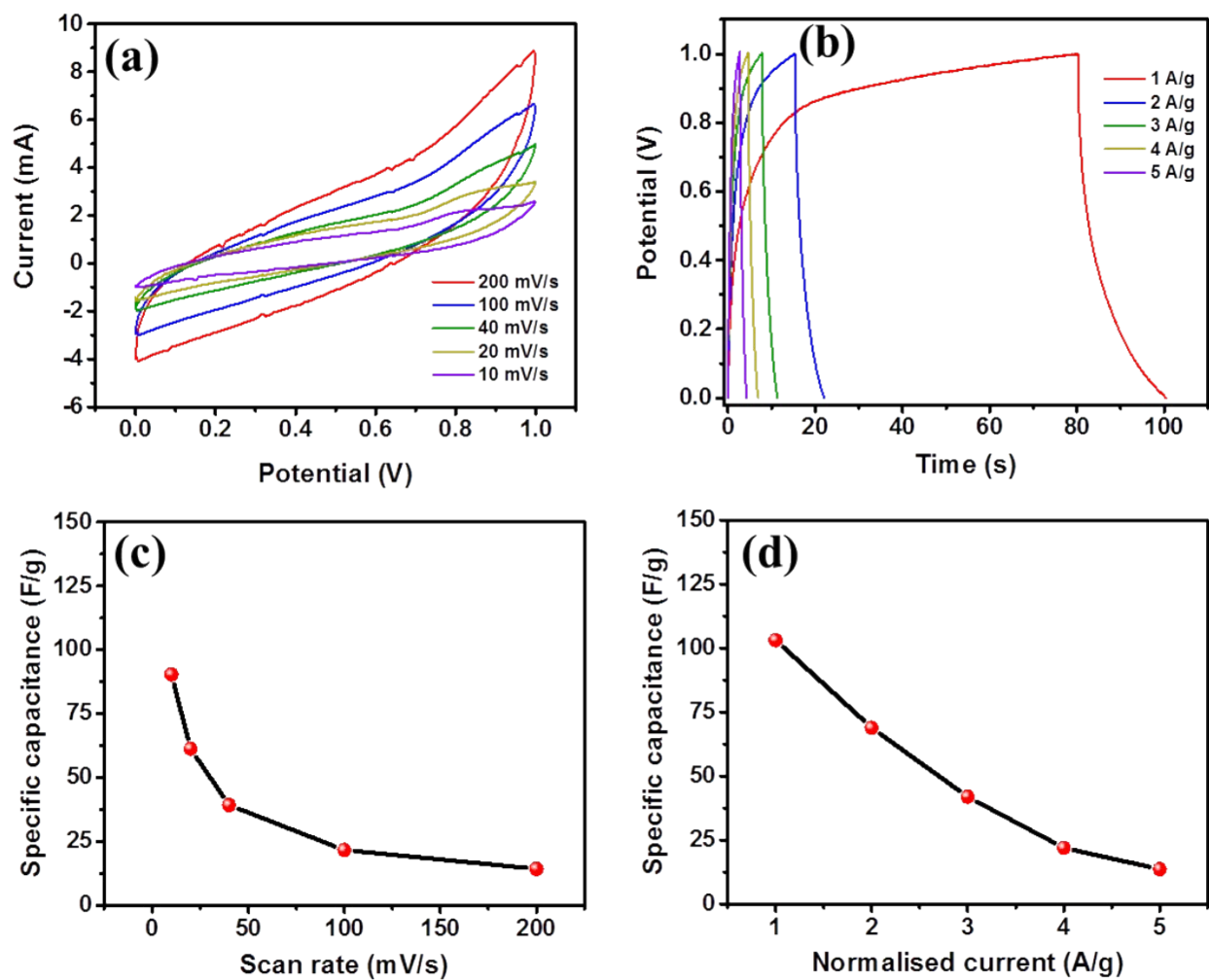


**Fig. S10** Supercapacitor data for  $VSe_2$  (a) Cyclic voltammetry curves at different scan rates, (b) charge-discharge curves at different values of normalized current, (c) plot of specific capacitance vs scan rate, (d) plot of capacitance vs mass normalized current.

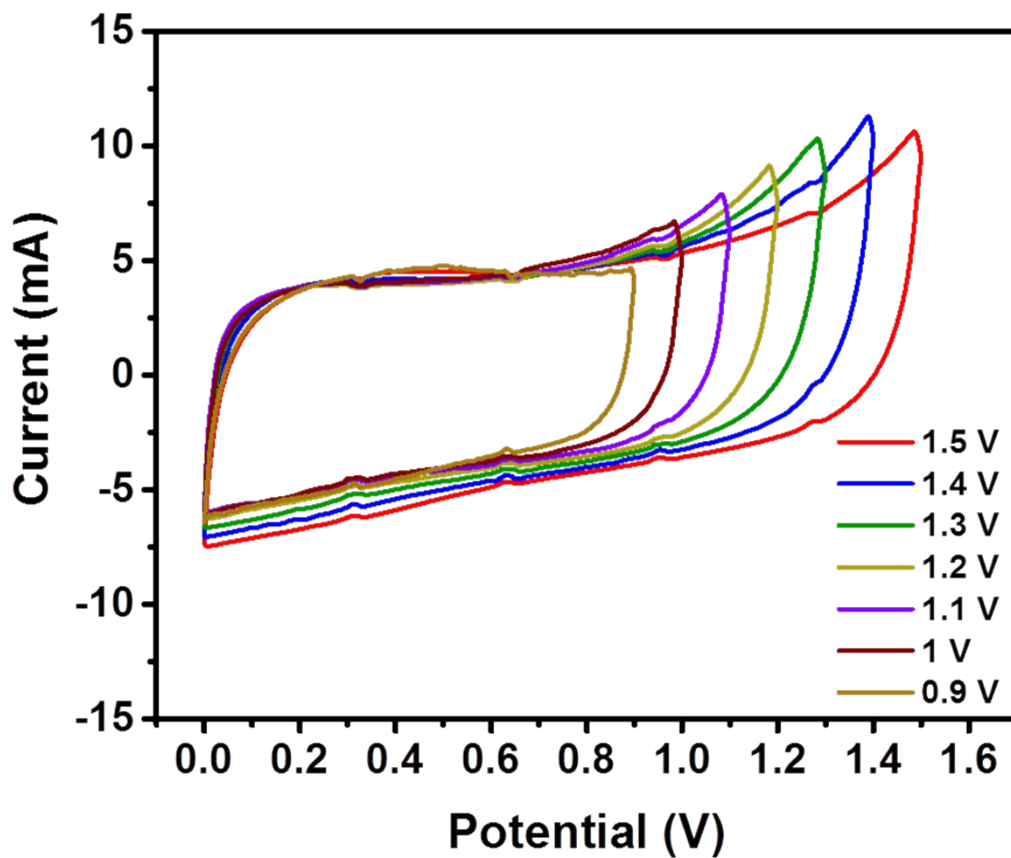


**Fig. S11** Comparison of cyclic voltammograms for RGO obtained at various working potential window. At ~1.1-1.2, onset of oxygen evolution process can be observed and therefore a working potential window of 1V was taken for measuring the supercapacitor performance of RGO.

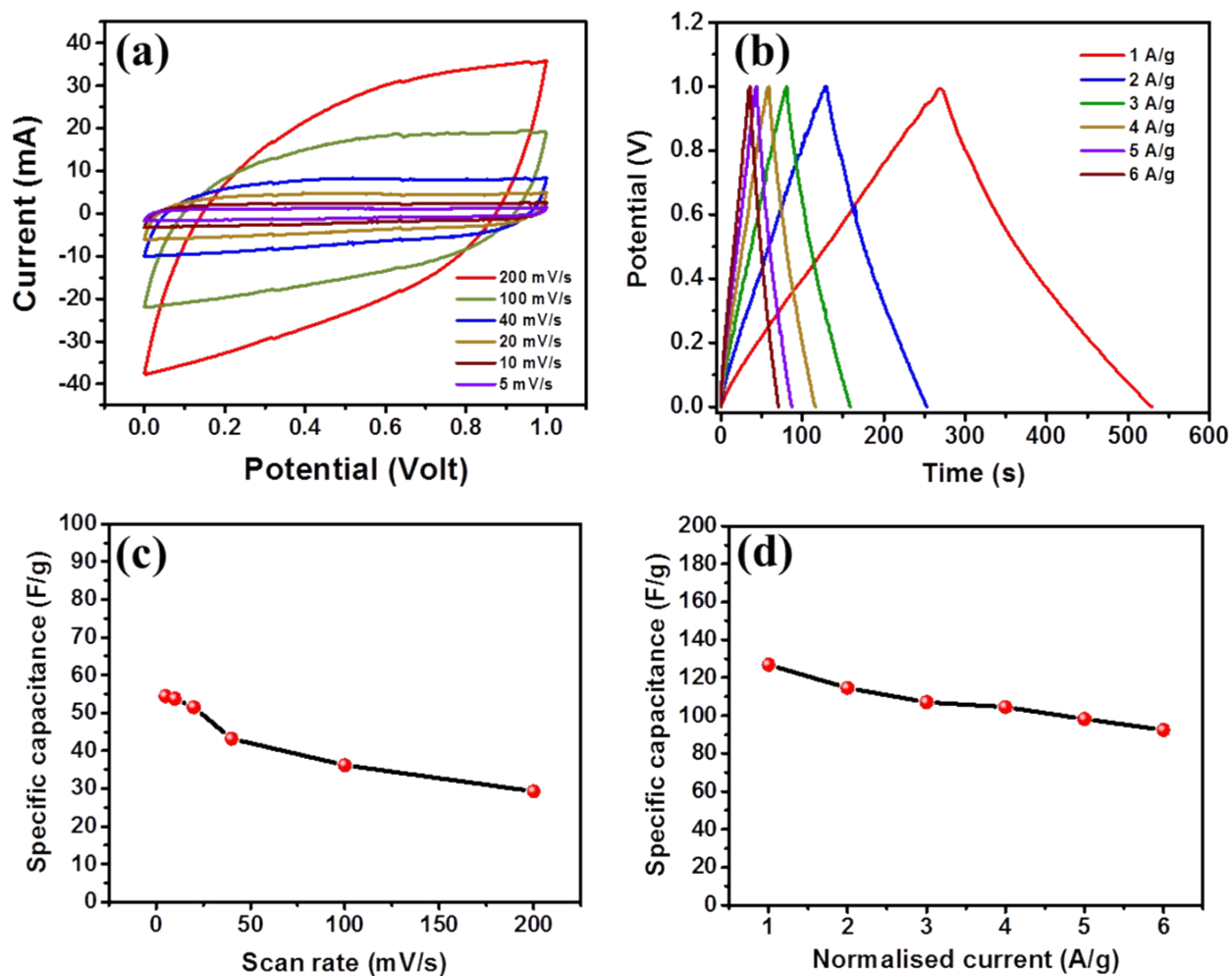


**Fig.S12** Supercapacitor data for RGO showing (a) cyclic voltammetry curves at different scan rates, (b) charge-discharge curves at different normalized currents, (c) capacitance vs scan rate and (d) capacitance vs mass normalized current.

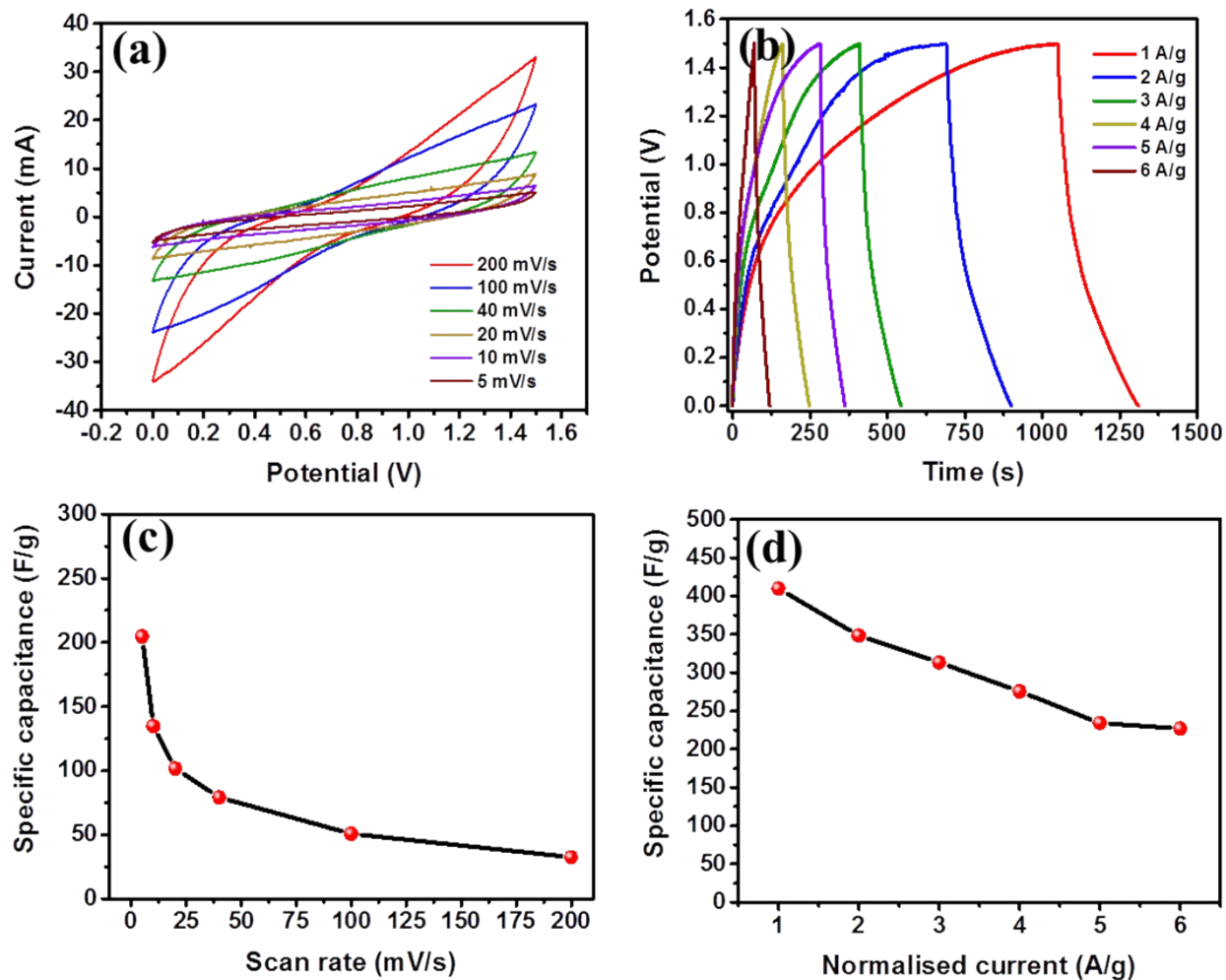


**Fig. S13** Supercapacitor data plot for V/G\_0.15 showing, (a) cyclic voltammety curves, (b) charge-discharge curves, and plots showing variation of capacitance with (c) scan rate and (d) mass normalized currents.

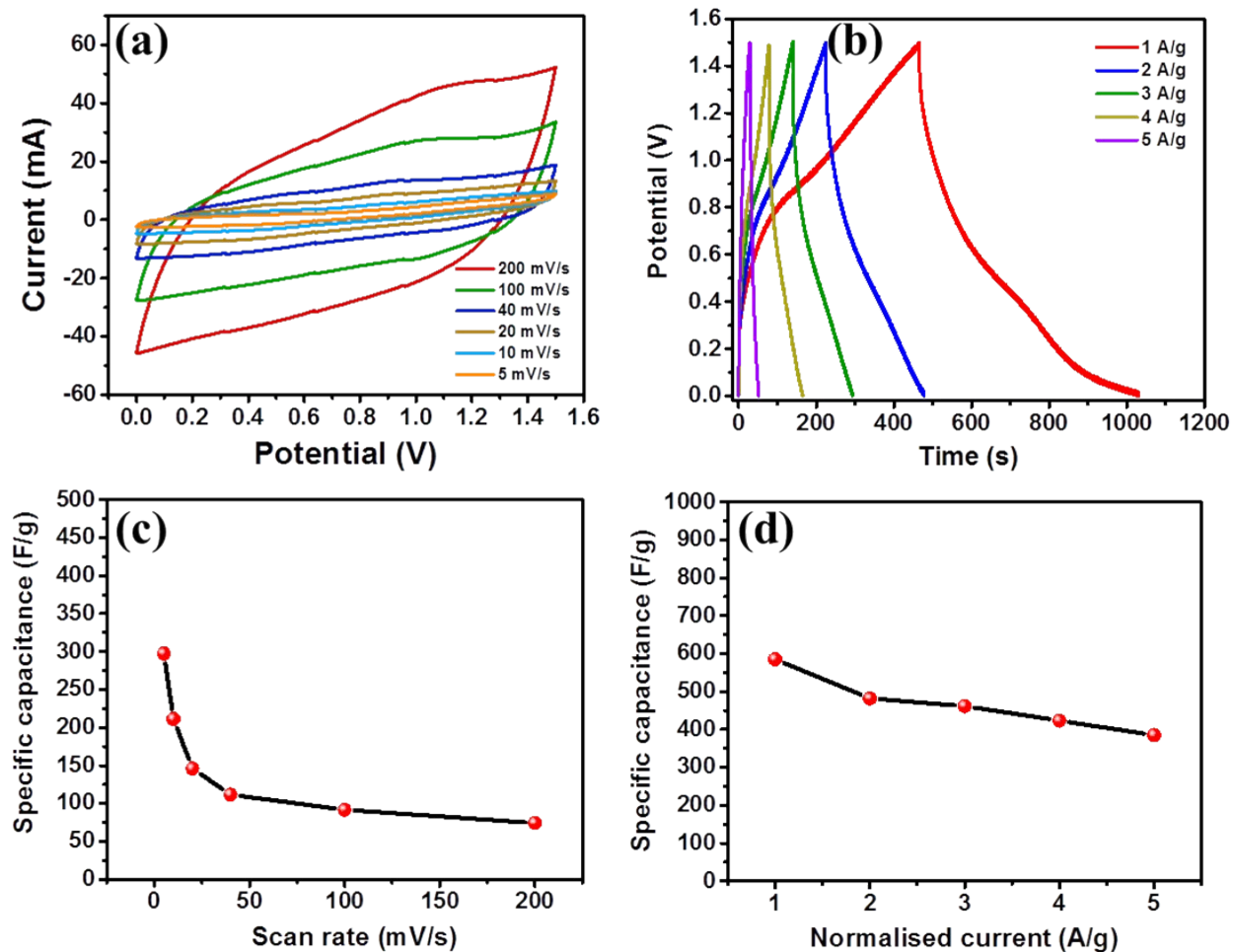


**Fig. S14** Supercapacitor data plot for V/G\_0.75 sample showing (a) cyclic voltammetry and (b) charge-discharge curves, (c) capacitance vs scan rate and (c) capacitance vs mass normalized current.

**Table. 1** Comparison of supercapacitor performance of RGO, VSe<sub>2</sub>, V/G (0.15, 0.3 and 0.75) hybrids.

Sample	Maximum calculated specific capacitance (F/g)	Maximum calculated energy density (Wh/kg)	Maximum calculated power density (kW/kg)
RGO	126.83	17.62	1.32
VSe <sub>2</sub>	103.19	14.33	4.5
V/G_0.15	409.73	128.04	5.1
V/G_0.3	680.27	212.58	3.3
V/G_0.75	585.03	182.82	4.8

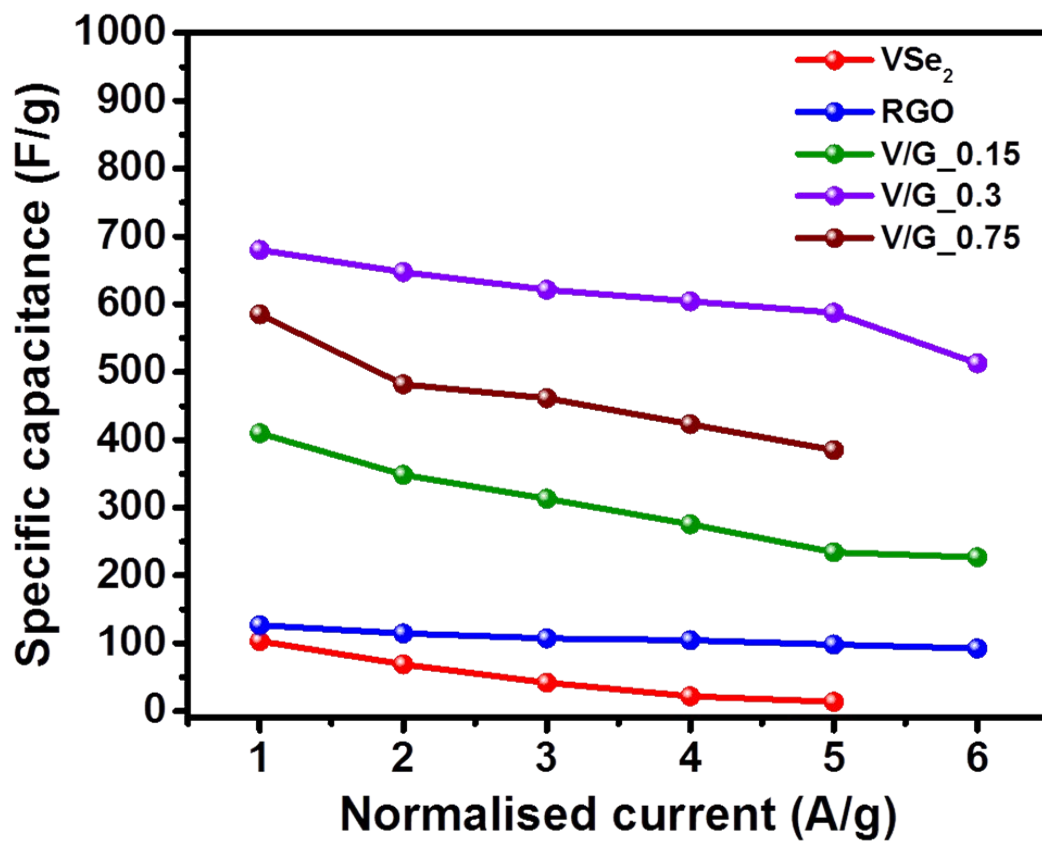


**Fig. S15** Comparison plot showing the variation of capacitance with current densities for VSe<sub>2</sub>, RGO, V/G\_0.15, V/G\_0.3 and V/G\_0.75 samples.

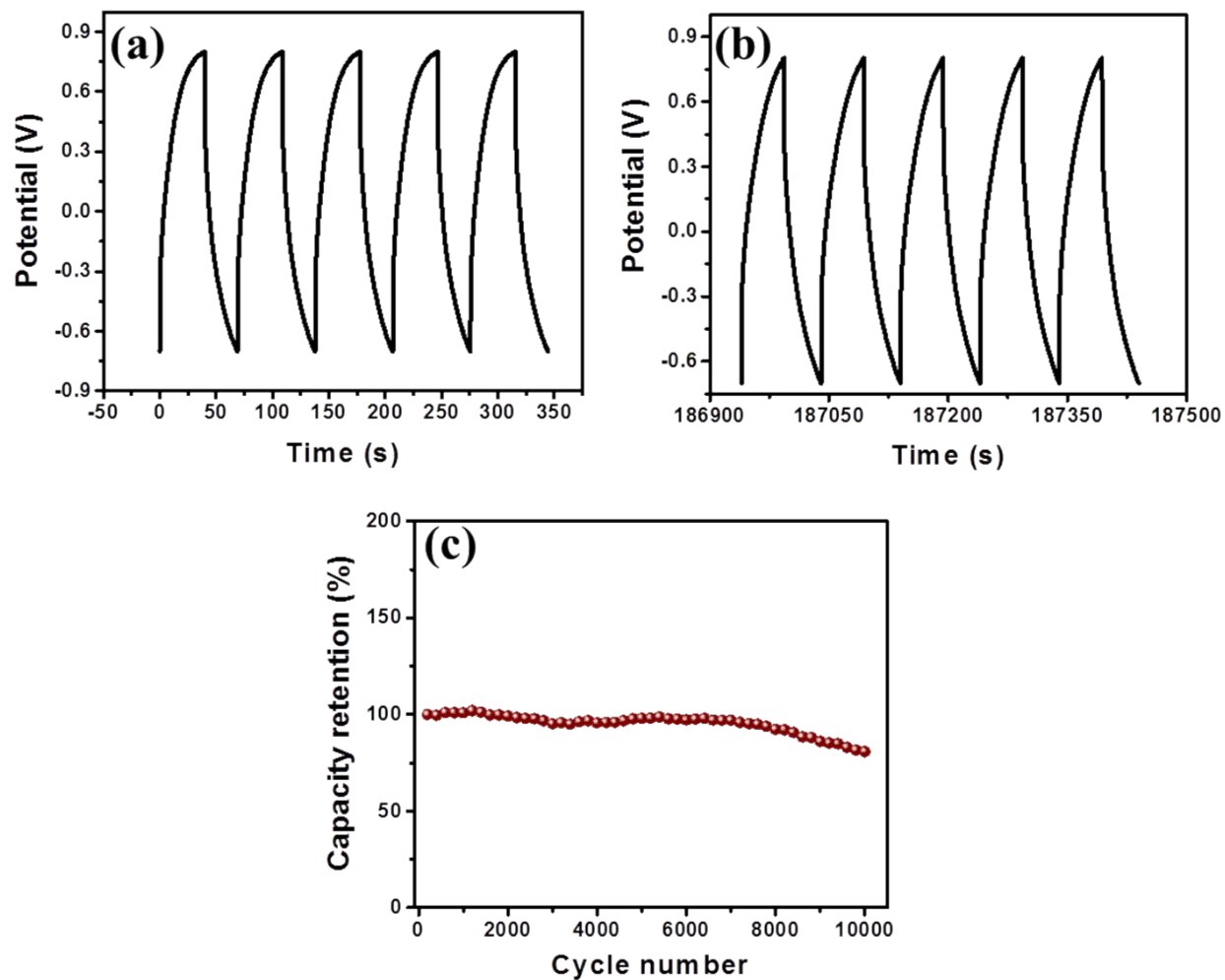


**Fig. S16** Stability test for V/G\_0.3 showing (a) first five cycles, (b) last five cycles, and (c) capacitance retention in percentage.

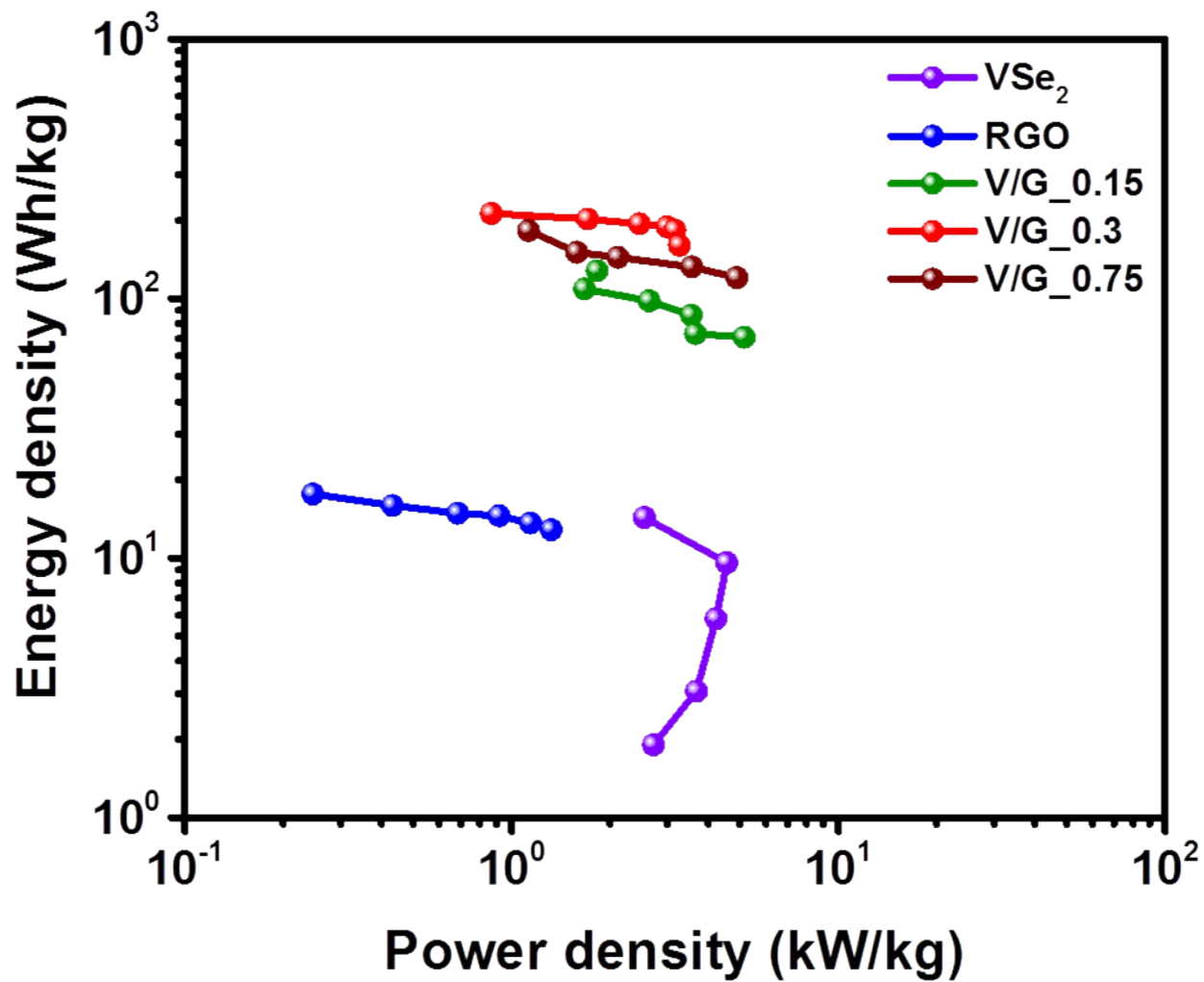
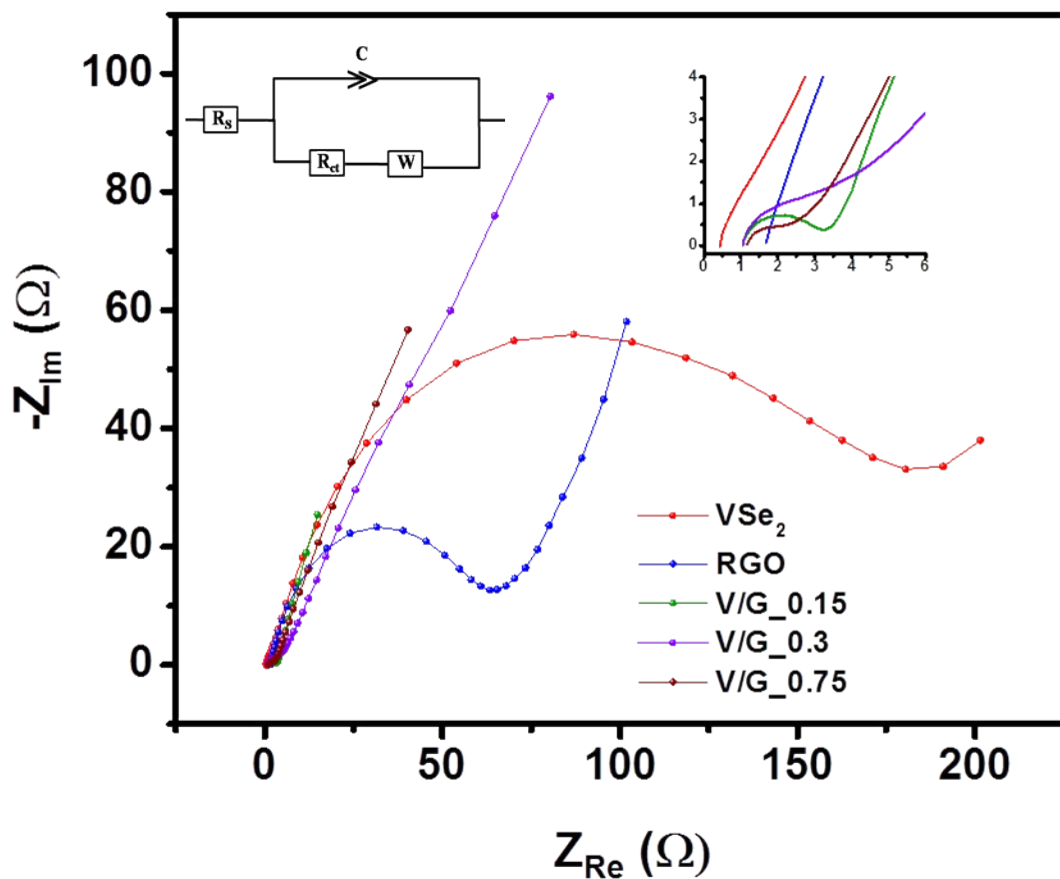


Fig. S17 Ragone plot showing energy density and power density relationship for VSe<sub>2</sub>, RGO, V/G\_0.15, V/G\_0.3 and V/G\_0.75 samples.



**Fig. S18** Nyquist plot showing charge-transfer resistances obtained from the supercapacitor devices having samples  $VSe_2$ , RGO, V/G\_0.15, V/G\_0.3, and V/G\_0.75. Inset shows the equivalent Randles circuit (left) which was used to fit all the spectra.  $R_s$  denotes the solution resistance,  $C$  is the capacitance resulting from double layer formation,  $R_{ct}$  is the charge-transfer resistance, and  $W$  is the Warburg element. A zoomed in portion of the plot (right) shows the  $R_{ct}$  properties of the composites.

**Table. 2**  $R_{ct}$  values of the samples obtained from the respective Nyquist plots

Sample Name	Charge transfer Resistance ( $R_{ct}$ )
VSe <sub>2</sub>	180 $\Omega$
RGO	62.3 $\Omega$
V/G_0.15	1.746 $\Omega$
V/G_0.75	1.677 $\Omega$
V/G_0.3	0.815 $\Omega$

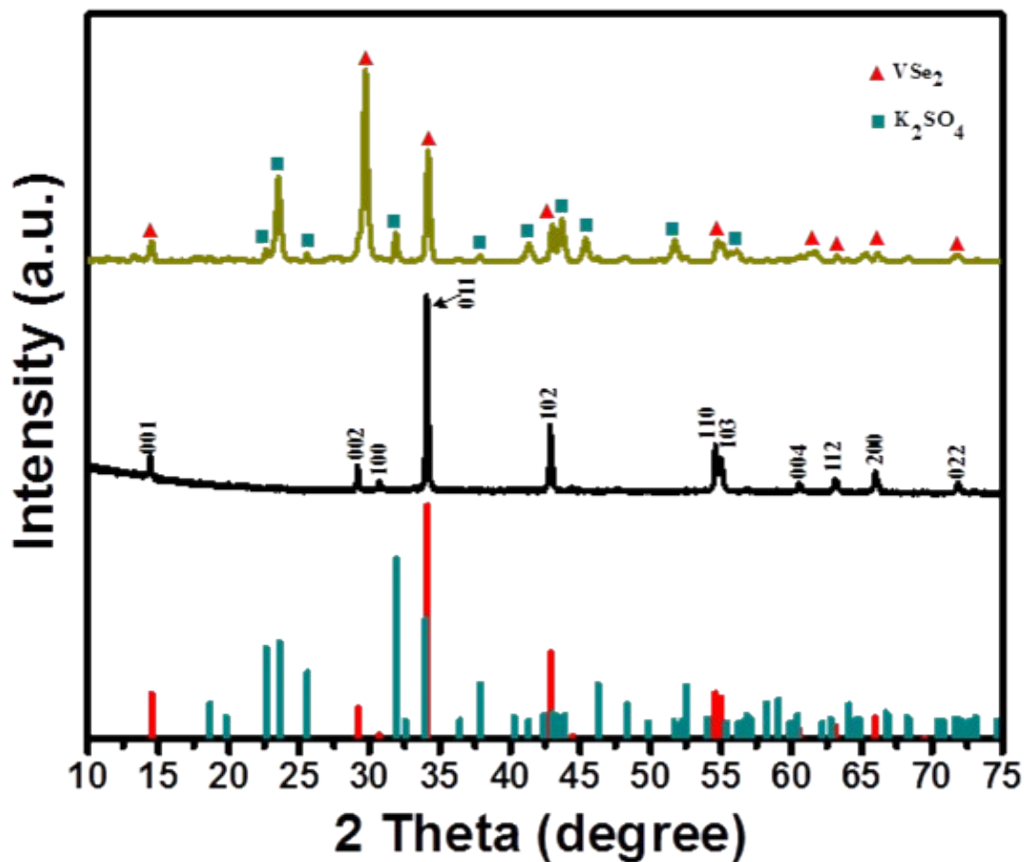


**Fig. S19** Comparison of X-ray diffraction spectra for  $\text{VSe}_2$  sample before (black) and after (dark yellow) the stability test. Peaks marked with red triangles are of  $\text{VSe}_2$  sample confirmed by matching with the JCPDS file (red column). Rest of the peaks marked with dark cyan squares matched with JCPDS file for  $\text{K}_2\text{SO}_4$  (dark cyan columns).

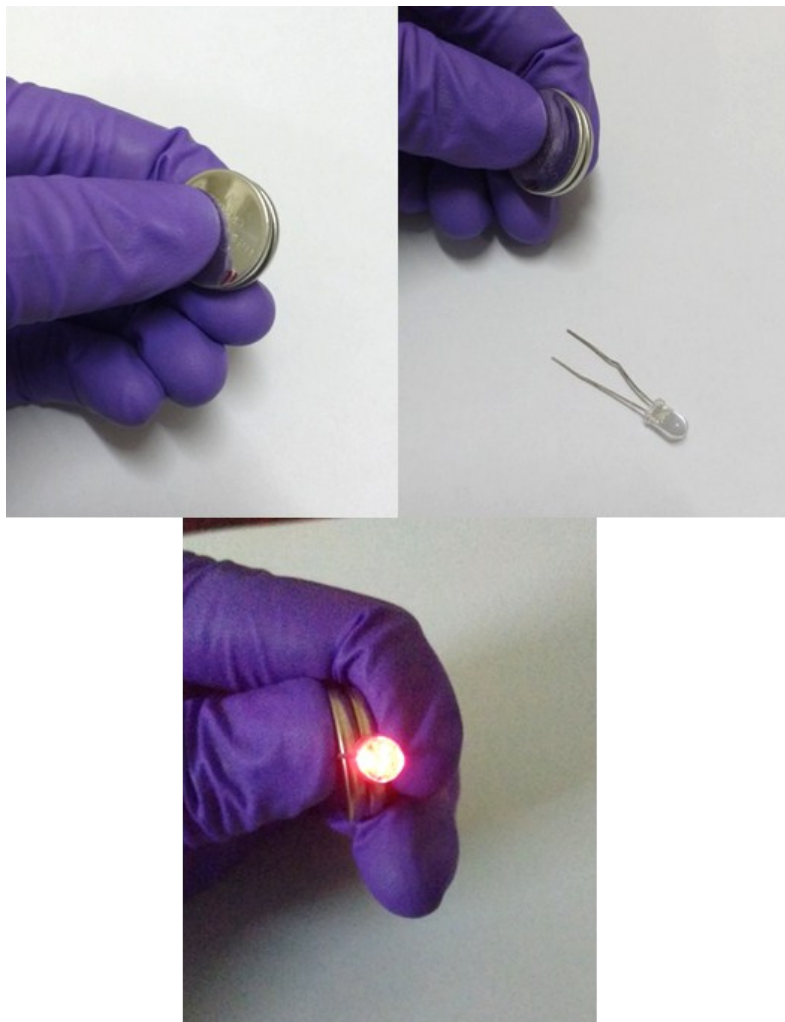


**Fig. S20** Optical image showing two CR2032 type coin cell (connected in series) having the V/G\_0.3 hybrid as the active electrode material in operation.

## References:

- 1 S. Ratha, S. R. Marri, J. N. Behera and C. S. Rout, *Eur. J. Inorg. Chem.*, 2016, **2016**, 259–265.
- 2 K. Xu, P. Chen, X. Li, C. Wu, Y. Guo, J. Zhao, X. Wu and Y. Xie, *Angew. Chemie - Int. Ed.*, 2013, **52**, 10477–10481.
- 3 S. Ratha, S. R. Marri, N. A. Lanzillo, S. Moshkalev, S. K. Nayak, J. N. Behera and C. S. Rout, *J. Mater. Chem. A*, 2015, **3**, 18874–18881.
- 4 Y. Li, H. Wang, L. Xie, Y. Liang, G. Hong and H. Dai, *J. Am. Chem. Soc.*, 2011, **133**, 7296–7299.
- 5 H. Wang, J. T. Robinson, G. Diankov and H. Dai, *J. Am. Chem. Soc.*, 2010, **132**, 3270–3271.
- 6 S. Chen, J. Zhu, X. Wu, Q. Han and X. Wang, *ACS Nano*, 2010, **4**, 2822–2830.
- 7 X. Feng, Z. Yan, N. Chen, Y. Zhang, Y. Ma, X. Liu, Q. Fan, L. Wang and W. Huang, *J. Mater. Chem. A*, 2013, **1**, 12818–12825.
- 8 S. H. Choi and Y. C. Kang, *Chem. – A Eur. J.*, 2014, **20**, 6294–6299.